Journal of Nuclear Materials 394 (2009) 9–19

Contents lists available at ScienceDirect

Journal of Nuclear Materials

journal homepage: www.elsevier.com/locate/jnucmat

Modeling texture evolution during uni-axial deformation of Zircaloy-2

F. Xu *, R.A. Holt, M.R. Daymond

Department of Mechanical and Materials Engineering, Queen's University, Kingston, Canada

ARTICLE INFO

Article history:
Received 29 August 2008
Accepted 14 July 2009

ABSTRACT

Texture development in zirconium reactor components greatly affects their in-service performance, in particular influencing dimensional stability, hydride induced cracking and fracture. Understanding texture evolution in terms of micromechanical deformation mechanisms contributes to improved engineering design of the components. The texture evolution during uni-axial deformation of Zircaloy-2 obtained using neutron diffraction was interpreted with a visco-plastic self-consistent model, based on an extensive data set achieved through *in situ* and *ex situ* neutron diffraction measurements. In the model, the influences of prism, basal, pyramidal⟨a⟩, pyramidal⟨c + a⟩ slip, tensile twinning, and hardening due to dislocation interactions were considered. Model parameters were adjusted to obtain a simultaneous 'best-fit' to the stress–strain curves, Lankford coefficients, development of peak intensities in three dimensions and post-deformation textures, for specimens compressed or pulled in three principal directions relative to the slab texture. The texture formation was found to be directly related to the activation of different deformation mechanisms. Pyramidal⟨a⟩ slip was unnecessary in the modeling. Accounting for interactions between deformation modes was critical to correctly predicting texture development and stress–strain curves. This study provides further understanding on the plastic deformation of Zircaloy-2.

© 2009 Elsevier B.V. All rights reserved.

1. Introduction

Zirconium (Zr) alloys are widely used in nuclear reactors due to their low thermal neutron capture cross-section, excellent corrosion-resistance in hot water, and good mechanical properties. The in-service behavior (e.g. delayed hydride cracking, dimensional stability and fracture) of Zr alloys strongly depends on the crystallographic texture (both macro- and microscopic) of the components, due to complex interactions between texture evolution and intergranular stress evolution (i.e. the stresses that develop among different grain orientations). Thus, it is necessary to understand the development of texture and intergranular stresses in order to control the anisotropy of mechanical properties and to predict the behavior of the material made by a new manufacturing route (e.g. the calandria tubes for the Advanced CANDU Reactor [1]). This demands sufficient knowledge of how texture develops during deformation and what deformation mechanisms (e.g. slip and twinning) are responsible for the development.

Zircaloy-2 has a stable α-phase (*hcp*) at room temperature [2] and is highly anisotropic in its thermal, elastic and plastic properties, both at the single crystal and polycrystal levels. The anisotropy at the single crystal level can lead to the formation of texture in the polycrystal during manufacturing. The understanding of operating deformation mechanisms in Zircaloy-2 is incomplete. At room temperature, it is well established that prism ⟨a⟩ slip (pr)$\{10\bar{1}0\}\langle 11\bar{2}0\rangle$ is the primary deformation mode and easiest to activate, while pyramidal ⟨c + a⟩ slip $\langle 11\bar{2}3\rangle$ (pyr⟨c + a⟩ or pyca) on the $\{10\bar{1}1\}$ or $\{11\bar{2}1\}$ plane, and/or tensile twinning $\{10\bar{1}2\}\langle 10\bar{1}1\rangle$ (ttw) must occur to accommodate the plastic deformation along the *c*-axis [3]. Including basal ⟨a⟩ slip (bas) $\{0001\}\langle 11\bar{2}0\rangle$ in polycrystalline modeling has been shown to help improve the agreement between the model and experiment for texture modeling [e.g. 4–7], but there is no direct experimental evidence for basal slip in *polycrystal* Zr alloys at *room* temperature, though under other circumstances it may occur [8–13]. No conclusive experimental evidence for pyramidal ⟨a⟩ slip (pyr⟨a⟩ or pya) or compressive twinning was found in the room-temperature deformation in Zr alloys, though some researchers have included them in the modeling to fit their experimental textures [e.g. 6,14–18]. The lack of experimental evidence for basal or pyr⟨a⟩ slip is principally due to the difficulty in unambiguously identifying the slip plane by transmission electron microscopy observations. More details concerning the occurrence of basal slip in Zircaloy-2 can be found in [19].

Deformation textures in α-phase Zr and its alloys made by various manufacturing processes have been reported extensively in the literature [e.g. 4,7,20–28]. Plenty of qualitative interpretations that relate to the macroscopic stress/strain states have been given [3,20,21,29–35]. Quantitative interpretations in terms of deformation mechanisms have also been developed, but only with limited success. The obstacles mainly arise from limited experimental data

* Corresponding author. Address: Department of Mechanical and Materials Engineering, Queen's University, 60 Union Street, Nicol Hall, Kingston, Ontario, Canada K7L 3N6. Tel.: +1 613 533 3236; fax: +1 613 533 6610.
E-mail address: xu@me.queensu.ca (F. Xu).

0022-3115/$ - see front matter © 2009 Elsevier B.V. All rights reserved.
doi:10.1016/j.jnucmat.2009.07.006

that failed to provide adequate constraints on the parameters used in the model, and the large number of undetermined model parameters (e.g. Critical Resolved Shear Stresses, or CRSSs, and hardening parameters). This is manifested by the widely varying derived single crystal properties reported in the literature, as summarized in [36]. For example, the derived ratio of the ⟨c + a⟩ slip CRSS to the prism slip CRSS varies dramatically from 1.8 [5] to 100 [32].

This paper aims to provide an extensive investigation of the texture development observed during room-temperature tension and compression of Zircaloy-2, and a further understanding of the micromechanics during the deformation, with the aid of a visco-plastic self-consistent model (VPSC) [17]. This complements our previous analysis [37] using an elasto-plastic self-consistent (EPSC) model [38] for interpretation of the internal strain development. The active deformation modes with their CRSSs, hardening and interaction parameters are identified to simulate the experiments.

Although the deformation textures we are investigating are induced by simple uni-axial loading, the parameters considered in the model and the data used to constrain the model are considerably more extensive than by previous authors. In the model, we considered the influence of prism slip, basal slip, pyr⟨a⟩ slip, pyr⟨c+a⟩ slip, tensile twinning and dislocation interactions. We introduced the *entire* set of experimental data (i.e. stress–strain curves, Lankford coefficients,[1] texture development, peak intensity development) as constraints on the model. This is significant, as the 'as-derived' single crystal properties are more likely representative of the 'actual material' than those derived using a small set of constraints.

2. Experimental procedures

The source material is a piece of 70 mm thick Zircaloy-2 slab. The composition is Zr, 1.43–1.45 wt.% Sn, 0.13–0.14 wt.% Fe, 0.1 wt.% Cr, 0.05 wt.% Ni, 1260–1440 wt ppm O, 150–160 wt ppm C. The slab was warm rolled at ~700 K, which induced recrystallization, and cooled to room temperature. The grains are nearly equi-axed with an average size of ~20 μm and have a very low dislocation density. As manufactured, most basal plane normals are orientated along the normal direction (ND), with a spread of ±50° towards the transverse direction (TD) and ±30° towards the rolling direction (RD). The $\{10\bar{1}0\}$ normals are moderately concentrated ±30° away from RD [39], Fig. 1.

In situ neutron diffraction measurements were performed for the nine tension tests at the L-3 beam line, the National Research Universal (NRU) reactor, Chalk River Laboratories (constant-wavelength source), and for the six compression tests at the Engin-X beam line, ISIS, Rutherford Appleton Laboratory (time-of-flight source), respectively. Dogbone-shaped tensile samples of 6.35 mm × 6.35 mm gauge cross-section and cylindrical compression samples 9 mm diameter × 18 mm long were cut relative to the three principal directions in the slab. These have allowed for the determination of peak intensity evolution in three dimensions for both tension and compression (all over 10%) along each of the three principal slab directions (i.e., rolling, transverse and normal). The gauge lengths of the samples have been chosen to ensure a uniform plastic deformation within the irradiated volume. Specifically, the tensile/compression tests were carried out under position (or stroke) control. After each incremental load, the sample was allowed to relax from the peak load reached. Data collection for neutron diffraction was then performed at ~90% of the peak load level [40]. The experimental details were reported in [40].

[1] Lankford coefficient (or *R*-ratio) is defined as the ratio of the plastic strains in the two Poisson directions during tension or compression. This coefficient directly reflects the macro-scale plastic anisotropy of a material [40].

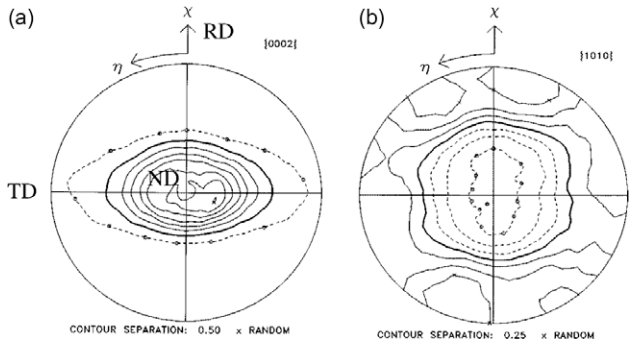

Fig. 1. Experimental pole figures of the Zircaloy-2 slab [39]: (a) $\{0\,0\,0\,2\}$ and (b) $\{10\bar{1}0\}$.

Eight peaks were measured during each of the compression tests, $\{0\,0\,0\,2\}$, $\{10\bar{1}3\}$, $\{10\bar{1}2\}$, $\{11\bar{2}2\}$, $\{10\bar{1}1\}$,$\{20\bar{2}1\}$, $\{11\bar{2}0\}$ and $\{10\bar{1}0\}$; due to the constraints of the monochromator, five peaks were measured during each of the tension tests, $\{20\bar{2}1\}$, $\{20\bar{2}0\}$, $\{11\bar{2}\bar{2}\}$, $\{11\bar{2}0\}$ and $\{0\,0\,0\,4\}$ (or $\{0\,0\,0\,2\}$). Stress–strain responses reported by clip gauges were recorded *in situ* during deformation on the stress rigs. Lankford coefficients were determined by measuring the permanent changes in macroscopic dimension (before and after deformation) along the two Poisson directions using a digital caliper. Pole figures (PFs) were subsequently measured using constant-wavelength neutron diffraction for the deformed specimens at the E-3 beam line at the NRU reactor. Microstructures were investigated. Electron back-scatter diffraction studies by scanning electron microscopy have revealed relatively large tensile twins, and high-resolution transmission electron microscopy observations have shown a significant number of fine tensile twins in the specimens compressed along RD, compressed along TD and pulled along ND [41]. No evidence of any type of compression twins was found.

3. Modeling

In the VPSC model, each grain is treated as a visco-plastic ellipsoidal inclusion embedded in, and interacting with, a homogeneous effective medium (HEM) that represents the polycrystal aggregate. The strength of interaction between the inclusion and HEM is represented by the interaction parameter n^{eff} [42]. This parameter was 10 in the calculations, representing a compromise between the rigid upper-bound approximation and softer approximations such as the tangent self-consistent model [43]. Each of the deformation modes was assumed to be fairly rate insensitive in order to represent the measurement stress state of the material, thus the stress exponent, n (the inverse of the strain rate sensitivity) was set to 20 [44]. The stress-relaxation process was not modeled.

The model allows for the hardening of individual deformation systems, described with an extended Voce hardening law [44]:

$$\tau^s = \tau_0^s + (\tau_1^s + \theta_1^s \Gamma)[1 - \exp(-\theta_0^s \Gamma/\tau_1^s)], \quad (1)$$

where τ^s is the instantaneous CRSS, τ_0^s and $\tau_0^s + \tau_1^s$ are the initial and final back-extrapolated CRSSs, respectively, θ_0^s and θ_1^s are the initial and asymptotic hardening rates, and Γ is the accumulated plastic shear in the grain.

The model also allows for 'self' and 'latent' hardening by introducing coupling coefficients $h^{s/s'}$ which empirically account for the obstacles that dislocations in system s' represent to the propagation of dislocations in system s [17]:

$$\Delta\tau^s = \frac{d\tau^s}{d\Gamma}\sum_{s'} h^{s/s'}\Delta\gamma^{s'}, \quad (2)$$

where $\Delta\gamma^{s'}$ is the increment of shear strain in deformation system s', and $\Delta\tau^s$ is the resultant gain in the instantaneous CRSS.

The occurrence of twinning can significantly change the texture by reorienting the twinned volumes relative to the matrix, facilitating or hindering the activation of easier slip mode such as prism slip. Twinning also introduces effective barriers for the propagation of dislocations and for the activation of other twins [45–47]. This barrier effect on slip and twinning systems are described empirically by Eq. (2).

The contribution of twinning to texture development in VPSC has been described with various models such as the predominant twin reorientation (PTR) scheme, and the volume fraction transfer scheme [16]. The PTR scheme is used in this paper. Within each grain, the twinned volume fraction is monitored with respect to the shear strain. The sum over all twin systems of a certain kind and over all grains represents the accumulated twin fraction V^{acc} in the aggregate. After each strain step, the grains are polled randomly to check whether or not the volume fraction of the predominant twinning system exceeds a threshold value. If so, the entire grain is reoriented to a new orientation reflective of this reoriented crystallite and is then added to a quantity 'effective twinned fraction (V^{eff})'. This polling process continues until either all the grains are checked in a random order or V^{eff} exceeds V^{acc} [16]. The twinned grains are prohibited to undergo a second reorientation by twinning. Grain reorientation by twinning is prevented until a threshold value A^{th1} is accumulated in any given system (typically 10–25% of grain volume) and rapidly raises the threshold to a value around $A^{th1} + A^{th2}$ (typically 50–60% of grain volume) [16]. In this work, A^{th1} and A^{th2} were treated as fitting parameters.

The initial texture of the Zircaloy-2 slab is represented by an aggregate of 15,456 discrete orientations ($5^\circ \times 5^\circ \times 5^\circ$ grid in the Euler space). Being equi-axed as observed experimentally, each grain is represented by a spherical inclusion (which is a special case of ellipsoidal inclusions because the grains are equi-axed), with the properties of the medium determined by averaging over all the grains. The boundary condition was set to uni-axial compression or tension, with an incremental strain step of 0.001.

Four slip and twinning modes are considered initially: prism slip, basal slip, pyr⟨c+a⟩ slip on the plane $\{10\bar{1}1\}$ and tensile twinning. The influences of pyr⟨a⟩ slip and other types of ⟨c+a⟩ slip will be discussed in Section 5.1. The Voce hardening parameters, τ_0, τ_1, θ_0 and θ_1, and the latent hardening parameters, for each of the four modes were treated as fitting parameters. Due to the large number of fitting parameters, testing the validity of all the parameter combinations against the experimental data is impractical. A possible way is to use a numerical optimization method to automatically find the best set. However, such a method has its own computational demands and complications (e.g. avoiding false minima) and is not available at present. Here, the parameter set was determined through iterative 'manual' fitting of the experimental data. This task was in part fulfilled by taking advantage of the initial texture, which allows the hardening parameters of particular deformation modes to be tuned in a relatively independent manner.

The ranges ([minimum–maximum] GPa) of τ_0 given in [19] for each of the slip modes are considered: [0.09–0.11] for prism slip, [0.14–0.17] for basal slip, and [0.32–0.36] for pyr⟨c+a⟩ slip. The range of τ_0 for tensile twinning was selected as [0.18–0.28] GPa. The parameters were incremented in coarse (0.1 GPa) and subsequently fine (0.05 and 0.01 GPa) steps for each of the CRSSs and hardening parameters. Detailed descriptions on the parameter selection process are given in [36]. Briefly, a coarse texture model ($10^\circ \times 10^\circ \times 10^\circ$ grid in the Euler space) was used at first. The fitting parameters were separated into several different groups, each tested with their impact on each of the fitting objectives. The six loading cases were divided into the 'slip' and 'twin' groups, based on the relative amount of experimental evidence for twinning. The parameters were fitted to the 'slip'-group cases first, and then adjusted to fit the 'twin'-group. The model was then refined with a finer texture mesh, i.e. $5^\circ \times 5^\circ \times 5^\circ$ grid (15,456 grain orientations) and parameters were finely tuned. The parameters giving rise to the 'best-fit' with the whole experimental data set are listed in Tables 1 and 2. It is emphasized that we used this single set of material parameters in the model to fit the complete experimental data set.

From the model the macroscopic stress–strain responses, texture, and activities of individual deformation modes, as well as the relative intensity of diffraction peaks in a particular sample direction can be determined. Both the experimental intensity and calculated volume fraction data were normalized to the pre-deformation texture in each of the three principal directions, i.e. to the initial texture coefficient (multiples of random distribution – m.r.d.) for each diffraction peak.

4. Comparison with experiments

4.1. Macroscopic mechanical responses

Fig. 2 displays the calculated macroscopic stress–strain curves superimposed with the experimental data, for compression and tension tests along the three principal directions of the slab. The experimental data represent the averaged stress and strain states corresponding to the neutron diffraction measurements. Note that the starting points in the calculated curves do not overlap the experimental ones. This is because the VPSC model excludes elasticity which does not contribute to the macrotexture development, and the basic formula in the model do not allow for a 'zero' stress. This also leads to the failure in reproducing the elastic–plastic transition region. In the fully-plastic region (>∼1.5% total strain), the model reasonably captures the stress–strain curve for each of the six loading cases.

The fact that the highest yield stress occurs for loading along ND (with most *c*-axes), the lowest for loading along RD (with nearly no *c*-axes), and an intermediate value for loading along TD can be explained qualitatively in terms of texture of the original slab. Deformation along ND and, less so, TD requires the activation of either ⟨c + a⟩ slip or twinning to deform along the *c*-axis. Deformation along RD requires mainly ⟨a⟩ slip which is much easier to activate.

Table 1
Critical resolved shear stresses and Voce hardening parameters.

	τ_0 (GPa)	τ_1 (GPa)	θ_0	θ_1
prism<a> slip	0.100	0.030	0.50	0.08
basal<a> slip	0.155	0.001	0.01	0.00
pyr<c + a> slip	0.320	0.130	0.80	0.40
Tensile twinning	0.220	0.020	0.15	0.08
	$A^{th1} = 0.15$	$A^{th1} + A^{th2} = 0.60$		

Table 2
Parameters describing latent hardening due to dislocation interactions ('1' means isotropic hardening).

System *s*	$h^{s/pr}$	$h^{s/bas}$	$h^{s/pyca}$	$h^{s/ttw}$
prism<a> slip	2	1	1	12
basal<a> slip	1	1	1	1
pyr<c + a> slip	1	1	2	1
Tensile twinning	1	1	1	2

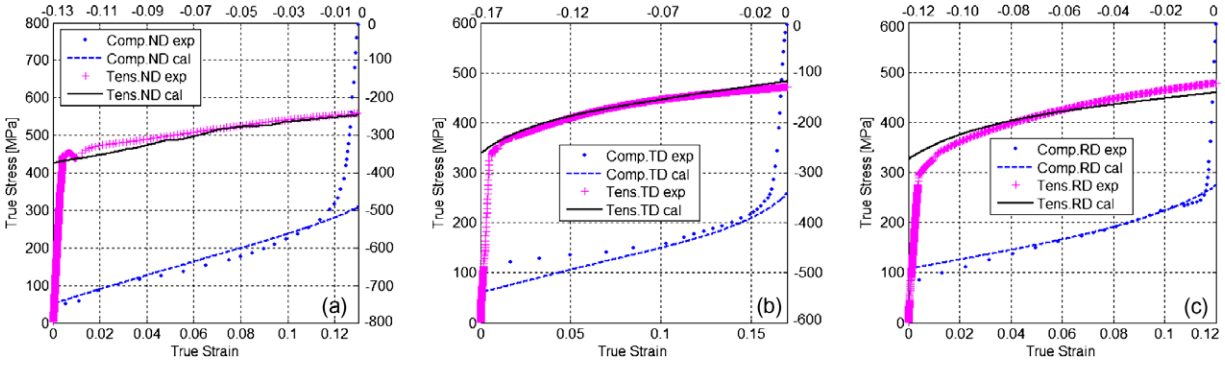

Fig. 2. Experimental and calculated stress–strain curves compression and tension along (a) ND, (b) TD, and (c) RD.

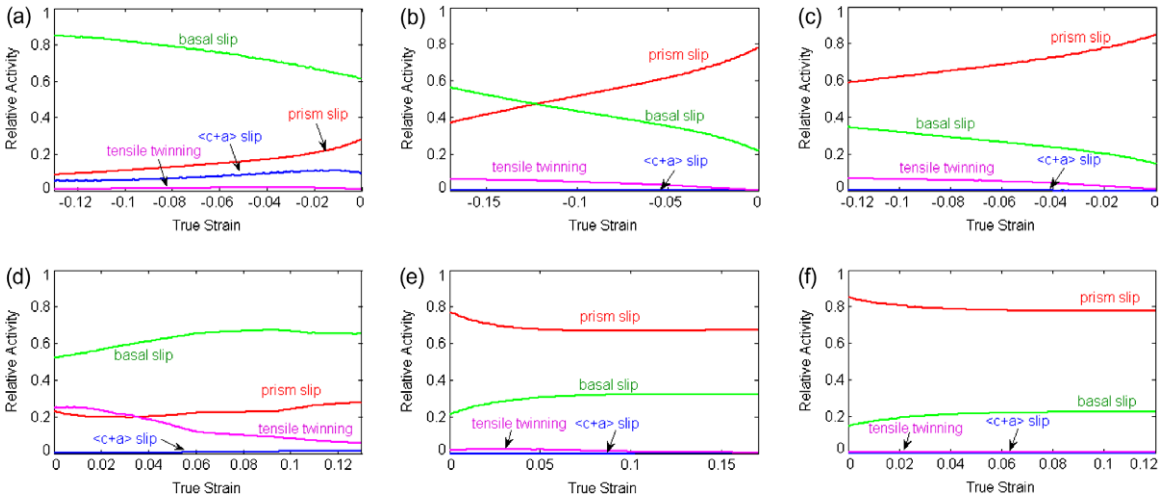

Fig. 3. Relative activities of the deformation systems for (a) Comp.ND, (b) Comp.TD, (c) Comp.RD, (d) Tens.ND, (e) Tens.TD and (f) Tens.RD.

Examining the calculated relative activities (i.e. relative plastic strains accommodated) of individual deformation modes (Fig. 3) offers a clearer understanding of the macroscopic responses.

The modeling shows significant pyr⟨c + a⟩ slip activity in Comp.ND,[2] while in Tens.ND, tensile twinning is abundant. The activity contributed by prism and basal slip in Comp.ND is largely similar to that in Tens.ND. Thus the higher yield stress in Comp.ND than that in Tens.ND is attributed to the higher CRSS for pyr⟨c + a⟩ slip than that for twinning. The higher hardening rate in Comp.ND than that in Tens.ND is due to the quicker hardening of the⟨c + a⟩ slip than the other modes (i.e. θ_1 is much higher for pyr⟨c + a⟩ than that for the other modes, Table 2), and possibly the lack of tensile twinning as a stress-relaxation mechanism in Comp.ND.

Negligible twinning and ⟨c + a⟩ slip are predicted in Tens.TD and Tens.RD; instead, tension along these two directions is mainly accommodated by prism and basal slip, with a higher relative activity of basal slip in Tens.TD. The higher yield stress for Tens.TD is explained by the higher CRSS for basal slip than that for prism slip, and the lower hardening rate in Tens.TD is possibly due to the slower hardening of basal slip as compared to prism slip (as indicated by their θ_1 values shown in Table 2).

The stress–strain curves for the compression and tension tests along TD are nearly identical (with reversed signs). However, they can be explained in terms of different deformation mechanisms operating (see Fig. 3); this also indicates that simply reproducing the stress–strain curves is insufficient to allow interpretation of deformation modes. In Comp.TD, the model reveals that the non-negligible twinning activity introduces obstacles to prism slip, reducing the prism slip activity at large strains. A qualitatively similar hardening rate in Comp.TD and Tens.TD occurs because Tens.TD has a higher activity of prism slip (hardens more quickly than basal slip), but Comp.TD has more twins (present obstacles to prism slip). Similar explanations can be applied to the stress–strain curves observed in compression and tension along RD.

The 'best-fit' model well reproduces the Lankford coefficients (or the degree of macroscopic plastic anisotropy), with the highest in Tens.TD, followed by that in Tens.RD, Comp.TD, Comp.RD and Tens.ND or Comp.ND (Table 3, 'best').

4.2. Development of texture

Figs. 4–9 compare the calculated and experimental development of the texture coefficients in terms of multiples of a random distribution (mrd) in three dimensions for all the measured crystallographic planes. In general the figures show agreement between the model and experiments which is acceptable for each of loading cases. The developing trends for all the crystallographic planes, especially for those showing gradual and monotonic changes in texture coefficient, are well captured. However, the agreement is less satisfactory for some of the basal and prism planes in the cases where significant twinning is involved, e.g. {0 0 0 2} in Comp.RD/ND and Tens.ND/ND.

[2] Comp.ND (or Tens.ND) represents compression (or tension) along ND, and so on for the other directions.

Table 3
Comparison of predicted Lankford coefficients with experiments (note: 'Cal.' represents the model results. The 'best'-'pr+bas+pyca+ttw' set represents the coefficients calculated using the 'best-fit' parameters given in Tables 1 and 2).

	Tens.ND $\varepsilon_{RD}:\varepsilon_{TD}$	Tens.TD $\varepsilon_{RD}:\varepsilon_{ND}$	Tens.RD $\varepsilon_{TD}:\varepsilon_{ND}$	Comp.ND $\varepsilon_{RD}:\varepsilon_{TD}$	Comp.TD $\varepsilon_{RD}:\varepsilon_{ND}$	Comp.RD $\varepsilon_{TD}:\varepsilon_{ND}$
Experimental	1.13	3.46	2.61	1.01	2.29	1.42
Cal. –VPSC 'best' 'pr + bas + pyca + ttw'	1.01	3.05	2.74	1.32	2.16	1.58
Cal. –VPSC* 'pr + pya + pyca + ttw'	1.05	7.50	4.48	2.18	9.94	4.54
Cal. –VPSC*'Iso-LH'**	1.02	2.98	2.80	1.25	2.30	2.02

* Will be discussed in Section 5.
** Iso-LH: isotropic latent hardening, i.e. all $h = 1$.

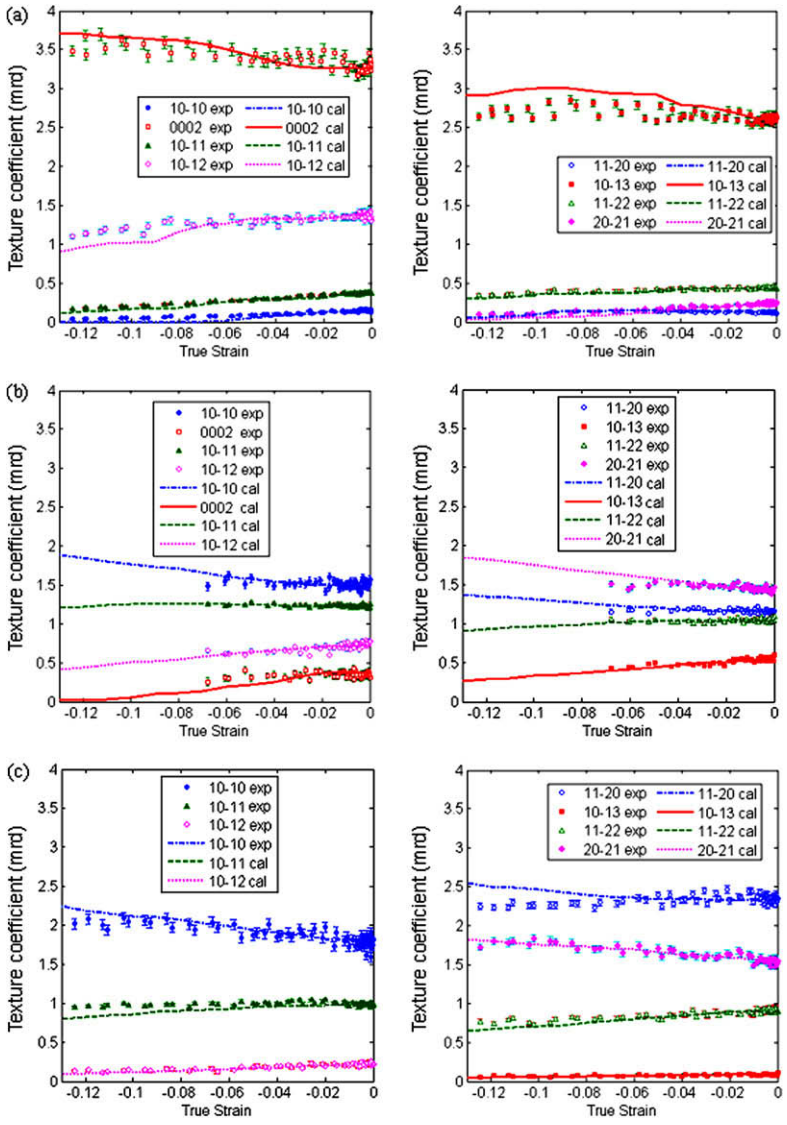

Fig. 4. Development of texture coefficients for compression along ND (test direction/measured direction): (a) ND/ND, (b) ND/TD and (c) ND/RD.

Predicted textures using the model parameters listed in Tables 1 and 2 are compared with their experimental counterparts in Figs. 10 and 11. In general, the model qualitatively captures the main features of the PFs, i.e. the positions of the *maximum* and *minimum* concentrations of the texture components and major changes associated with tensile twinning. The predicted textures are sharper in most cases. This is partially due to the assumption of the uniform response of the HEM in the model [48]. According to the 'homogeneity' assumption, grains in the same orientation should behave in the same manner. In a physical polycrystal, however, grains in the same orientation are very unlikely to interact with a group of surrounding grains which possess the same properties, thus grains in

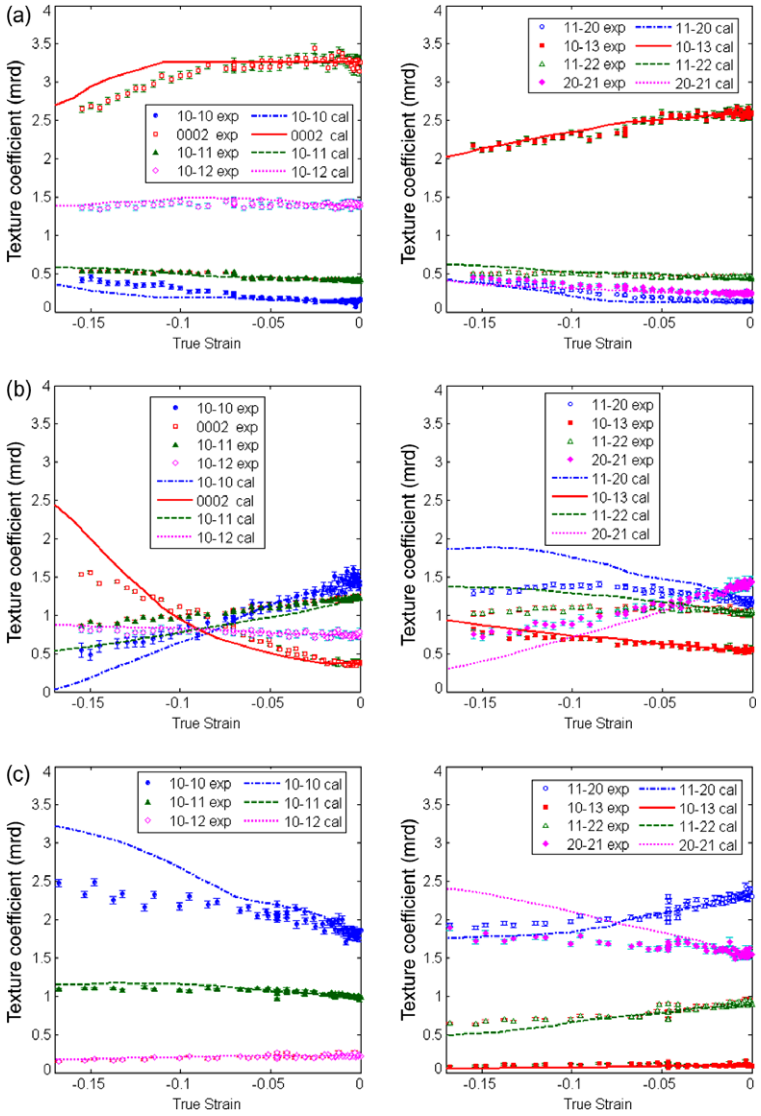

Fig. 5. Development of texture coefficients for compression along TD: (a) TD/ND, (b) TD/TD, and (c) TD/RD.

the same orientation should be reoriented differently. This would result in a greater spread in the final positions for one orientation and thus relatively milder texture, as opposed to the predictions. In Figs. 10 and 11, the calculated PFs with certain deformation modes inactive are also shown, which can help understand the texture formation. The texture development can be understood as the following by comparing the PFs.

(1) Comp.ND
1. The initial maximum $\{1\,0\,\bar{1}\,0\}$ concentrations around RD are strengthened. This is due to prism slip, without which the maximum concentrations will move to other positions.
2. More basal normals cluster close to ND than initially, but in general the basal normal distribution around ND does not change significantly. Basal slip reorients basal normals towards ND while the $\langle c + a \rangle$ slip does the opposite. These two slip modes work to roughly maintain the original basal normal distribution.

(2) Comp.TD and Tens.RD
1. The sixfold symmetry about ND of the $\{1\,0\,\bar{1}\,0\}$ lobes at the PF rim is brought about by prism slip.
2. The basal normal spread around ND expands in the ND-TD plane, but contracts in the ND-RD plane. This is caused by basal slip.
3. The appearance of the basal normals near TD in Comp.TD is induced by tensile twinning.
4. The split of the basal normal spread near ND towards TD in Comp.TD is controlled by basal slip.

(3) Comp.RD and Tens.TD
1. The sixfold symmetry about ND of the $\{1\,0\,\bar{1}\,0\}$ lobes at the PF rim is brought about by prism slip.
2. The basal normal spread around ND contracts in the ND-TD plane, but expands in the ND-RD plane. This is caused by basal slip.
3. The appearance of the basal normals near RD in Comp.RD is induced by tensile twinning.

(4) Tens.ND
1. $\{1\,0\,\bar{1}\,0\}$ maxima are tilted towards ±60° from ND in the ND-RD by prism slip.
2. The basal normal distribution around ND spreads more towards TD than towards RD as a result of basal slip (due to the more difficult deformation along TD, especially at the early stage of plastic deformation), with the central maximum splitting into two maxima in the ND-

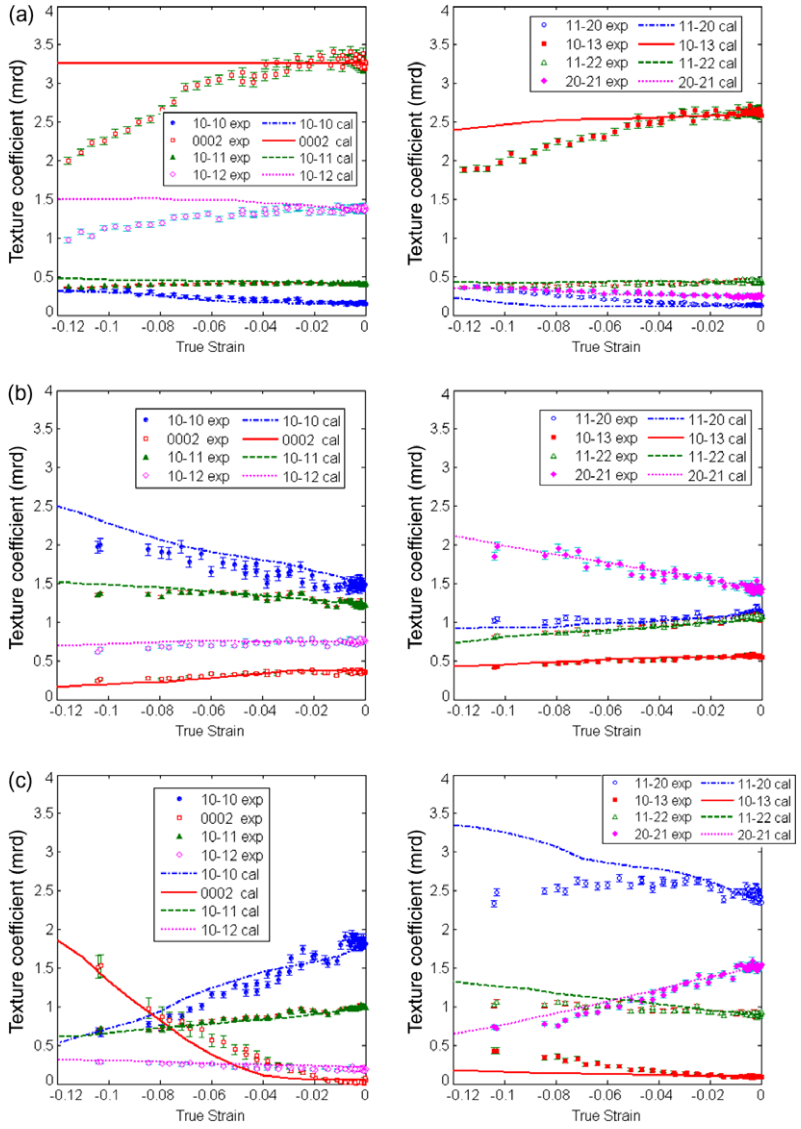

Fig. 6. Development of texture coefficients for compression along RD: (a) RD/ND, (b) RD/TD, and (c) RD/RD.

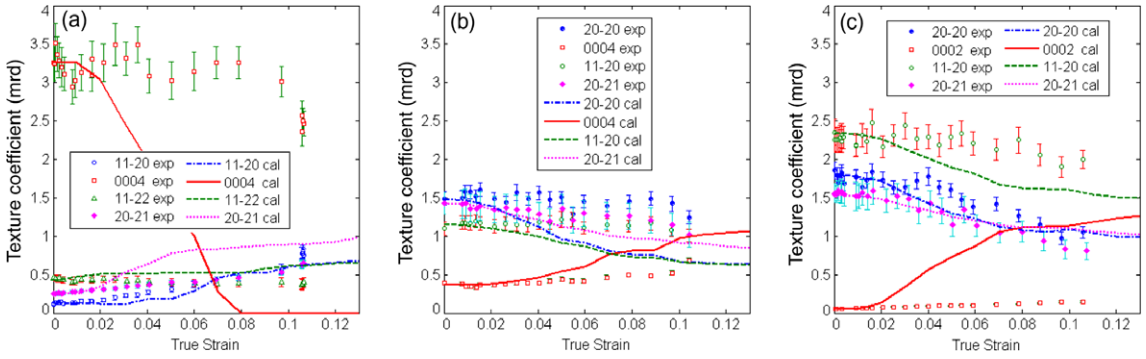

Fig. 7. Development of texture coefficients for tension along ND: (a) ND/ND, (b) ND/TD, and (c) ND/RD.

TD plane. This has resulted in the discontinuous distribution of the twinned basal grains around RD, i.e. most near RD but only a few exactly *along* RD. Accordingly, $\{10\bar{1}0\}$ normals around RD are twinned to the ND-TD plane, again with a discontinuous distribution.

5. Discussion

In Section 4, the influences of prism slip, basal slip, $\langle c + a \rangle$ slip and tensile twinning were considered, simultaneously achieving acceptable agreement between the model and experiments for

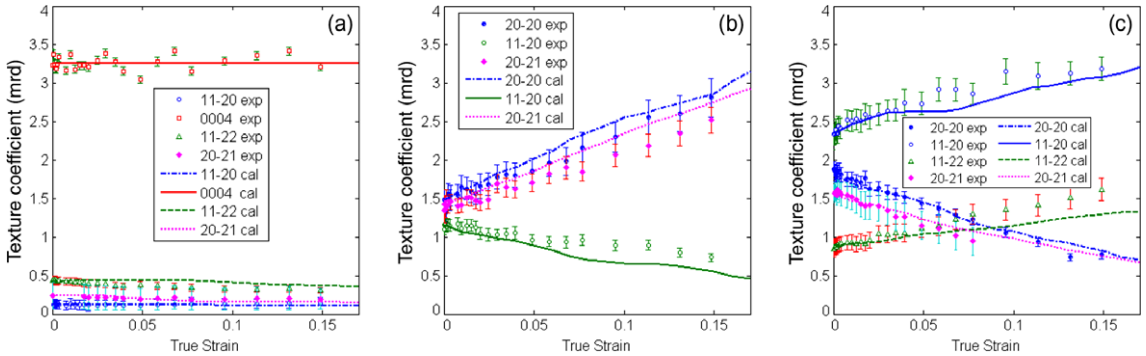

Fig. 8. Development of texture coefficients for tension along TD: (a) TD/ND, (b) TD/TD, and (c) TD/RD.

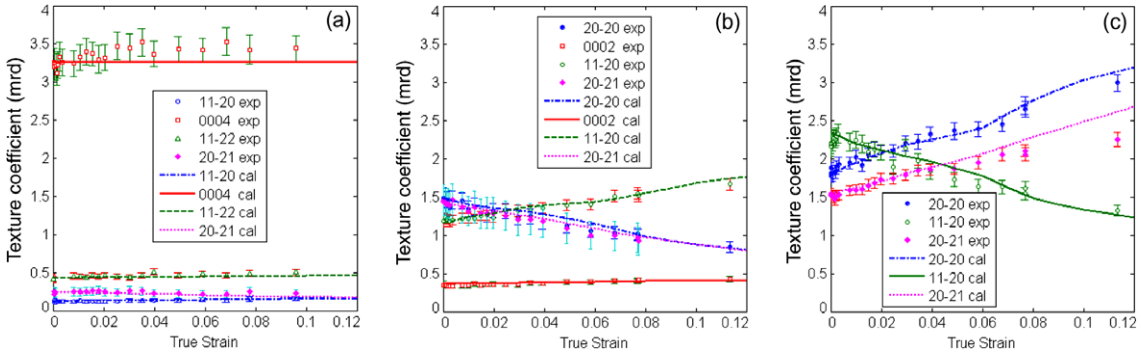

Fig. 9. Development of texture coefficients for tension along RD: (a) RD/ND, (b) RD/TD, and (c) RD/RD.

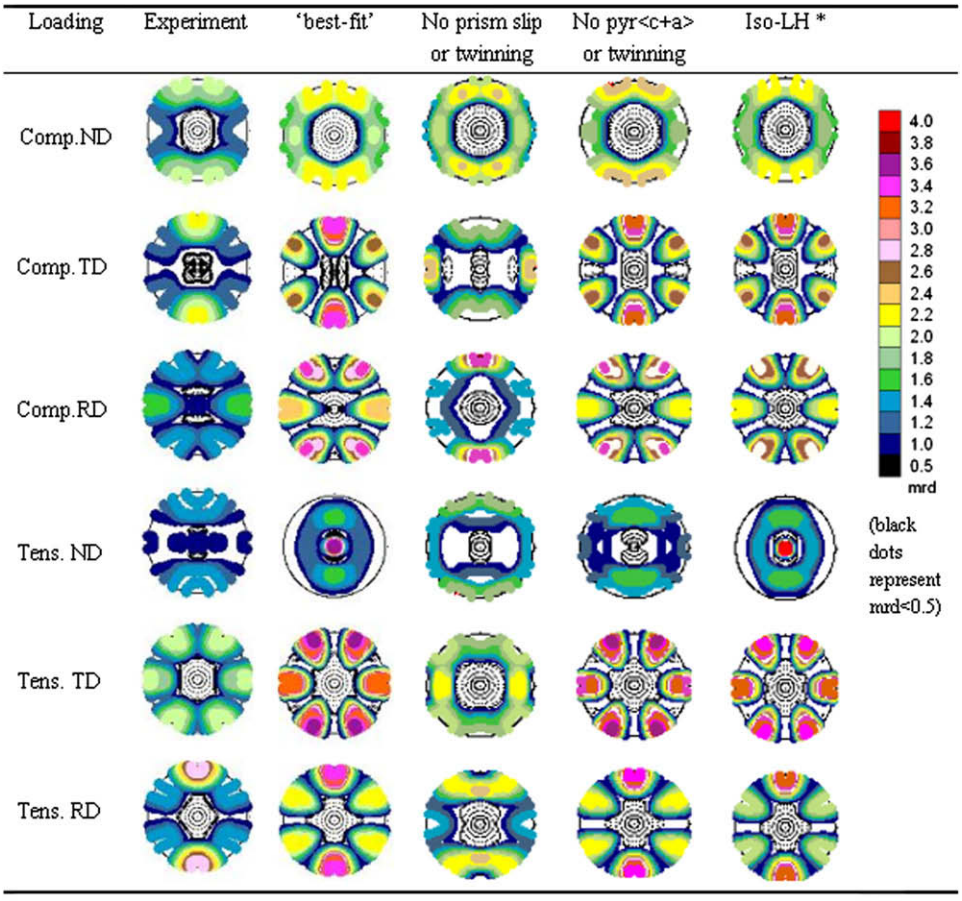

Fig. 10. Comparison of the predicted $\{10\bar{1}0\}$ pole figures with experiments.

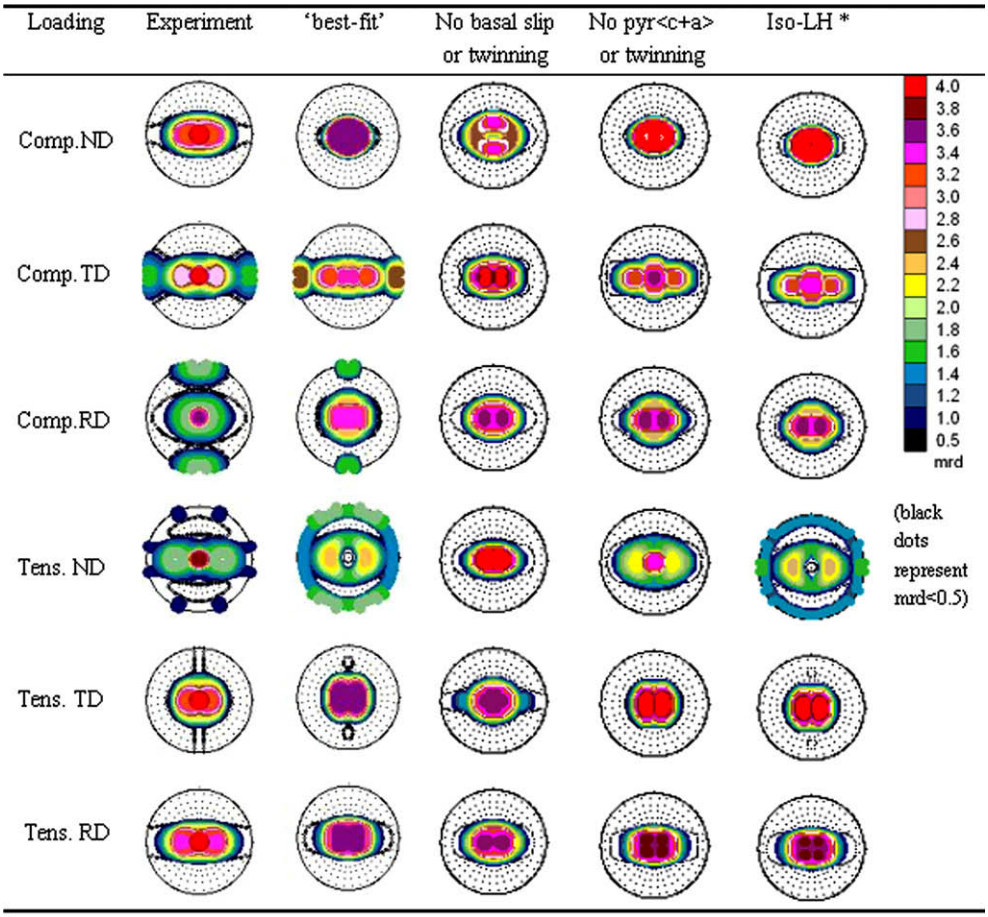

Fig. 11. Comparison of the predicted {0 0 0 2} pole figures with experiments.

each of the loading cases, in terms of the stress–strain curve, Lankford coefficient, post-deformation texture and development of texture coefficient. The importance is stressed of simultaneously arriving at acceptable fit to both macroscopic responses (e.g. stress–strain curves and Lankford coefficients) and microscopic behavior (i.e. texture coefficient development and post-deformation texture). Most previous texture modeling work only considered the final texture and/or stress–strain curves for specimens deformed in one or two directions. The Lankford coefficients and the history of peak intensity (or texture coefficient) changes have never previously been treated as fitting constraints in texture modeling. The significance of considering *anisotropic* latent hardening due to interactions between deformation modes ('slip–slip' and 'slip–twinning') is also stressed. This has been realized previously [e.g. 4,49]; however, in practice, such hardening effects have seldom been studied, because the data sets used have been too small to constrain a large number of parameters leading to ambiguity as to the uniqueness of the parameters so obtained. The anisotropic barrier effect of twinning on slip/twinning was accounted for by several workers [e.g. 50], but that of 'slip–slip' interaction has never been considered. The introduction of the whole experimental data set allows to constrain a large number of parameters, lending confidence to the derived characteristics of the active deformation mechanisms.

In this section, we will discuss the influences of the theoretical activation of pyr⟨a⟩ slip and other types of ⟨c + a⟩ slip. We will investigate the influences brought about by the dislocation interactions and tensile twinning. At last we will compare the derived single crystal material properties with those previously derived by use of an elasto-plastic.

5.1. Possible activation of pyr⟨a⟩ and other types of pyr⟨c+a⟩ slip

The effect of pyr⟨a⟩ slip is illustrated by replacing basal slip with pyr⟨a⟩ slip in the 'best' parameter set. Basal, rather than prism slip has been replaced for two reasons. First, prism slip is the primary deformation mode and must occur. Second, some other workers (see Section 1) have chosen pyr⟨a⟩ rather than basal slip for their modeling.

A combination of $\tau_0^{pr} = 0.08$, $\tau_0^{pya} = 0.15$, $\tau_0^{pyca} = 0.25$ and $\tau_0^{ttw} = 0.17$ GPa can result in acceptable stress–strain curve and final texture for each of the six loading cases, simultaneously. However, the predicted Lankford coefficients deviate far from experiments (Table 3), and they cannot be improved by simply tuning the parameters without including basal slip. This test clearly highlights the importance of considering Lankford coefficients as modeling constraints. Although a highly active pyr⟨a⟩ slip can simulate part of the roles of basal slip in reorienting basal normals, to achieve reasonable Lankford coefficients, τ_0^{pya} must be set as low as 0.05 GPa, which is unreasonable as it is even much lower than τ_0^{pr}, which is the lowest from experimental evidence [10]. Hence, while it is essential to include basal slip, it is not necessary to include pyr⟨a⟩ in the model; its effect being similar to a combination of prism and basal slip (mainly prism slip). This is consistent with previous con-

clusions [37] based on the development of internal strains in the material.

Replacing the pyr⟨c + a⟩ slip on $\{1\,0\,\bar{1}\,1\}$ with the slip on $\{1\,1\,\bar{2}\,1\}$ or $\{1\,1\,\bar{2}\,2\}$ plane (using the same CRSS) will produce very similar results to those shown in Section 4.2, with respect to both macro- and microscopic responses. Thus the possible activation of the ⟨c + a⟩ slip on $\{1\,1\,\bar{2}\,1\}$ or $\{1\,1\,\bar{2}\,2\}$ plane cannot be ruled out through modeling.

5.2. Influences of anisotropic latent hardening effects

Interactions between deformation modes (leading to latent hardening effects, described by parameters $h^{s/s'}$ in the model) can greatly affect the model results, especially the texture development. Figs. 10 and 11 show the calculations with isotropic latent hardening effects (i.e. all $h^{s/s'} = 1$) resulting in poorer agreement with experimental textures, for Comp.TD, Comp.RD and Tens.ND. Reducing the CRSS for tensile twinning can help improve these texture predictions, but will result in unacceptable stress–strain curves. The latent hardening can also greatly affect the stress–strain curves and slightly, the Lankford coefficients (Table 3). Fig. 12 shows the predicted stress–strain curve for Tens.ND without any latent hardening effects included in the calculation. The prediction deviates far from the experiment. Increasing the θ_1 value for prism, basal or tensile twinning can improve the stress–strain curve prediction to a limited extent, but will result in unacceptable texture predictions for Tens.ND, Comp.TD and Comp.RD.

It is emphasized that the interaction induced hardening cannot be fully represented by simply adjusting θ_0 or θ_1. The strength of interaction is very dependent on the relative activities of each deformation system and varies significantly during deformation.

By testing a wide combination of parameters against experimental data, it was found that the importance of $h^{s/s'}$ varies greatly amongst the deformation systems, in decreasing order of importance: $h^{pr/ttw}$, $h^{ttw/ttw}$, $h^{pr/pr}$ and $h^{pyca/pyca}$. For the others, isotropic hardening (i.e. $h^{s/s'} = 1$) gives the best fit to the data. This may indicate that: (1) tensile twins build up strong obstacles to the propagation of prism slip and twinning, (2) prism slip is easily activated resulting in high density of ⟨a⟩ dislocations which are likely to interact with each other, and (3) pyr⟨c + a⟩ slip is likely to interact mostly with itself. A plausible explanation is that prism slip first interacts with itself resulting in local stress concentrations that may foster the activation of tensile twinning or pyr⟨c + a⟩ slip. The model also suggested that basal slip does not tend to interact with itself or with other slip systems, as the anisotropic latent hardening involving basal slip (i.e. $h^{bas/s'} \neq 1$) has resulted in worse predictions. However, these are derived from the modeling aspect, at present with no concrete experimental evidence in support.

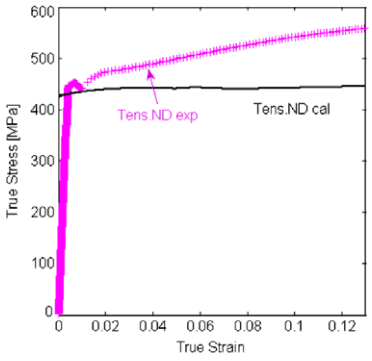

Fig. 12. Comparison of the stress–strain curve for the tension along ND. The calculation shows the huge deviation from the experiment when no latent hardening is considered.

5.3. Twinning activities

The agreement between the model and experiments, as to the development of peak intensity and final textures, is less satisfactory for the cases where substantial tensile twinning operates, especially for Tens.ND. This may be due to the inadequacy of the current twinning model (i.e. the PTR scheme). In Tens.ND, the model predicts more tensile twins around RD than observed in the experiment, with a nearly 100% depletion of basal normals near ND in the $\{0\,0\,0\,2\}$ PF and a substantial increase in $\{1\,0\,\bar{1}\,0\}$ normals near ND in the $\{1\,0\,\bar{1}\,0\}$ PF. This over-prediction is not fully understood. The VPSC model adopts the PTR scheme to deal with twinning such that a randomly polled grain, which is oriented favorably for twinning, will be *completely* twinned if the twinned fraction achieves a certain threshold value (15% of parent grain volume fraction in this work). Since initially there are a large number of grains suitable for twinning (i.e. the basal grains near ND), twinning is very active initially (see Fig. 3d) resulting in the rapid reduction of basal normals and substantial increase in $\{1\,0\,\bar{1}\,0\}$ normals near ND. In contrast, during compression along RD and TD, most of the plastic deformation can be accommodated by prism and basal slip; the twinning activity is relatively low (see Fig. 3b and c), and thus the depletion of basal normals and substantial increase in $\{1\,0\,\bar{1}\,0\}$ normals near ND are not induced.

5.4. Comparison with EPSC modeling results

In [37], we have used an EPSC model to interpret the lattice strain data, which were obtained along with the intensity data presented in this paper. Both EPSC and VPSC are self-consistent polycrystalline models that are based on the assumption of an Eshelby inclusion (stress and strain are uniform in the inclusion and linearly related to the applied stress and strain [51]) being surrounded by and interacting with the surrounding homogeneous effective medium (HEM). Thus it is expected that the single crystal properties derived from the two models should be largely consistent with each other. However, the models are different from each other as to the representation of the inclusion, interaction and HEM, for which EPSC uses an elasto-plastic description while VPSC uses a visco-plastic one. In addition, the results of the EPSC model are compared principally with the movement of diffraction peaks (i.e. internal strains), while the VPSC models is compared principally with changes in diffraction peak intensity (i.e. texture). Hence it is reasonable that the derived deformation mechanisms from the two models will not necessarily be the same.

Comparing the derived single crystal properties, it is found that both models have demonstrated that it is necessary to (1) include prism, basal, pyr⟨c + a⟩ slip, and tensile twinning (while pyr⟨a⟩ slip is unnecessary), (2) introduce Lankford coefficients to constrain the models, and (3) consider the anisotropic hardening effects due to deformation mode interactions. The two models have produced (1) close CRSSs (τ_0's) for the respective slip and twinning modes (2) similar trends as to the hardening behavior (θ_1) pertaining to either prism slip, basal slip or ⟨c + a⟩ slip, i.e. ⟨c + a⟩ slip hardens much more quickly than the ⟨a⟩ slip, (3) similar trends with respect to the relative activities of the contributing deformation modes under various deformation conditions relative to the parent plate, and (4) similar trends as to the latent hardening effects for most of the deformation mode interactions. The small discrepancies regarding the derived CRSSs and hardening parameters (e.g. hardening due to dislocation interactions) by the two models (see [37]) can be explained by their intrinsic differences and respective limitations.

The general consistency between the two models, in terms of the derived deformation mechanisms, the CRSSs and hardening

behavior, is significant – it strongly supports the conclusion that the derived single crystal properties are representative of the 'actual material', at least within the limitations of the models' ability to describe the material.

6. Conclusion

The texture development observed in rolled Zircaloy-2 slab pulled or compressed along the three principal directions, was interpreted with a visco-plastic self-consistent model. Prism slip, pyr⟨a⟩ slip, basal slip, pyr⟨c + a⟩ slip, tensile twinning, and the hardening due to dislocation interactions were considered in the model. Pyr⟨a⟩ slip was found to be unnecessary in the modeling, while the other modes are required. Accounting for hardening due to dislocation interactions was found to be critical in correctly modeling the texture formation.

A more extensive data set was used to constrain the modeling parameters than in the literature, i.e. in addition to the stress–strain curves and post-deformation textures and multiple testing directions, the Lankford coefficients and development of intensity for all the diffracting crystallographic planes were considered to constrain the model. The values of the parameters derived here must thus be considered more robust than those reported previously. This improvement in the modeling has refined the estimates of critical resolved shear stresses and hardening parameters, and for the first time provided estimates of the anisotropic latent hardening parameters, from the aspect of texture modeling.

Acknowledgements

The authors sincerely thank Dr. Carlos Tomé of Los Alamos National Laboratory for providing the VPSC code for texture modeling and Pole7 for the pole figure plotting. This work was sponsored by NSERC, COG, OPG and Nu-Tech Precision Metals under the Industrial Research Chair program in Nuclear Materials at Queen's University.

References

[1] J. Hopwood, in: Proceedings of 26th Annual Conference on Canadian Nuclear Society, 2005, Paper P23.
[2] R.G. Ballinger, G.E. Lucas, R.M. Pelloux, J. Nucl. Mater. 126 (1984) 53.
[3] E. Tenckhoff, ASTM STP 966 (1988) 1916 Race Street, Philadelphia.
[4] H. Francillette, B. Bacroix, M. Gaspérini, J.L. Béchade, Mater. Sci. Eng. A234–236 (1997) 974.
[5] H. Francillette, B. Bacroix, M. Gaspérini, J.L. Béchade, Acta Mater. 46 (1998) 4131.
[6] H. Francillette, O. Castelnau, B. Bacroix, J.L. Béchade, Mater. Sci. Forum 273–275 (1998) 523.
[7] A. Salinas Rodríguez, J.J. Jonas, Metall. Trans. 23A (1992) 271.
[8] J.E. Bailey, J. Nucl. Mater. 7 (1962) 300.
[9] J.I. Dickson, G.B. Craig, J. Nucl. Mater. 40 (1971) 346.
[10] A. Akhtar, Acta Metall. 21 (1973) 1.
[11] G.J.C. Carpenter, J.F. Watters, R.W. Gilbert, J. Nucl. Mater. 48 (1973) 267.
[12] K. Pettersson, J. Nucl. Mater. 105 (1982) 341.
[13] J.L. Martin, R.E. Reed-Hill, Trans. TMS AIME 230 (1964) 780.
[14] H. Francillette, O. Castelnau, B. Bacroix, J.L. Béchade, Mater. Sci. Forum 273–275 (1998) 523.
[15] R.A. Lebensohn, C. Tomé, Texture Microstruct. 14–18 (1991) 959.
[16] C.N. Tomé, R.A. Lebensohn, U.F. Kocks, Acta Metall. Mater. 39 (1991) 2667.
[17] R.A. Lebensohn, C. Tomé, Acta Metall. Mater. 41 (1993) 2611.
[18] P. Sanchez, A. Pochettino, Mater. Sci. Forum 495–497 (2005) 1597.
[19] F. Xu, R.A. Holt, M.R. Daymond, J. Nucl. Mater. 373 (2008) 217.
[20] R.G. Ballinger, The Anisotropic Behavior of Zircaloy-2, Garland, New York, 1979.
[21] D. Charquet, E. Alheritiere, G. Blanc, ASTM STP 939 (1987) 663.
[22] E. Tenckhoff, Metall. Trans. A 9 (1978) 1401.
[23] M.J. Philippe, F. Wagner, C. Esling, in: J.S. Kallend, G. Gottstein (Eds.), Proceedings of 8th International Conference on Texture of Materials, The Metallurgical Society, Warrendale, PA, 1988, pp. 837–842.
[24] B.A. Cheadle, C.E. Ells, Trans. TMS AIME 233 (1965) 1044.
[25] K.P. Steward, B.A. Cheadle, Trans. TMS AIME 239 (1967) 504.
[26] B.A. Cheadle, C.E. Ells, W. Evans, J. Nucl. Mater. 23 (1967) 199.
[27] E. Tenckhoff, Zeitschrift fuer Metallkunde 61 (1970) 64.
[28] E. Tenckhoff, P.L. Rittenhouse, Zeitschrift fuer Metallkunde 63 (1972) 83.
[29] V.M. Allen, M. Preuss, J.D. Robson, R.J. Comstock, Mater. Sci. Forum 495–497 (2005) 675.
[30] M.L. Picklesimer, Electrochem. Technol. 4 (1966) 289.
[31] E. Tenckhoff, J. ASTM Int. 2 (2005) 1.
[32] K.L. Murty, I. Charit, Prog. Nucl. Energy 48 (2006) 325.
[33] J.H. Keeler, W.R. Hibbard, B.F. Decker, Trans. Met. Soc. AIME 197 (1953) 932.
[34] J.H. Keeler, A.H. Geisler, Trans. Met. Soc. AIME 203 (1955) 57.
[35] K. Källström, Can. Metall. Quart. 11 (1972) 185.
[36] F. Xu, Ph.D. Dissertation, Queen's University, 2007.
[37] F. Xu, R.A. Holt, M.R. Daymond, Acta. Mater. 56 (2008) 3672.
[38] P.A. Turner, C.N. Tomé, Acta Metall. 42 (1994) 4143.
[39] F. Xu, R.A. Holt, R.B. Rogge, M.R. Daymond, in: Proceedings of 26th Annual Canadian Nuclear Society Conference, Toronto, Ontario, Canada, 2005, Paper T42.
[40] F. Xu, R.A. Holt, M.R. Daymond, R.B. Rogge, E.C. Oliver, Mater. Sci. Eng. A 488 (2008) 172.
[41] I.A. Yakubtsov, unpublished data, 2006.
[42] C.N. Tomé, Mod. Sim. Mater. Sci. Eng. 7 (1999) 723.
[43] S.R. Agnew, M.H. Yoo, C.N. Tome, Acta Mater. 49 (2001) 4277.
[44] C.N. Tomé, G.R. Canova, U.F. Kocks, N. Christodoulou, J.J. Jonas, Acta Metall. 32 (1984) 1637.
[45] L.M. Howe, J.L. Whitton, J.F. McGurn, Acta Metall. 10 (1962) 773.
[46] G.C. Kaschner, C.N. Tomé, R.J. McCabe, A. Misra, S.C. Vogel, D.W. Brown, Mater. Sci. Eng. A 463 (2007) 122.
[47] G.C. Kaschner, C.N. Tomé, I.J. Beyerlein, S.C. Vogel, D.W. Brown, R.J. McCabe, Acta Mater. 54 (2006) 2887.
[48] D.W. Brown, S.P. Abeln, W.R. Blumenthal, M.A.M. Bourke, M.C. Mataya, C.N. Tomé, Metall. Mater. Trans. 36A (2005) 929.
[49] A. Salinas Rodríguez, J.J. Jonas, in: J.S. Kallend, G. Gottstein (Eds.), Proceedings of International Conference on Texture of Materials, The Metallurgical Society, Warrendale, PA, 1988, p. 499.
[50] C.N. Tomé, P.J. Maudlin, R.A. Lebensohn, G.C. Kaschner, Acta Mater. 49 (2001) 3085.
[51] J.D. Eshelby, Proc. Roy. Soc. A241 (1957) 376.